APPENDIX A: TABLES

Table A1: Summary of white dwarf sample

System	Source (WD properties)	Type	Mass /$M_\odot$	T_{eff} /K	log(g /ms^{-2})	IR Excess
G166-58	Gianninas et al. (2011), IR excess from Farihi et al. (2008)	H	0.58	7390	7.99	Y
G241-6	Jura et al. (2012) (T, logg), Bergeron et al. (2011) (mass), Zuckerman et al. (2010) (IR excess)	He	0.71	15300	8	N
G29-38	Xu et al. (2014), IR excess from Zuckerman & Becklin (1987)	H	0.85	11800	8.4	Y
GALEX1931+0117	Koester et al. (2014), Vennes et al. (2010) (IR excess)	H	0.573	21457	7.9	Y
GALEXJ2339	Klein et al. (2021)	He	0.548	13735	7.93	N
GD362	Leggett et al. (2018), Becklin et al. (2005) and Kilic et al. (2005) (IR excess)	He	0.551	10057	7.95	Y
GD378	Klein et al. (2021)	He	0.551	15620	7.93	N
GD40	Coutu et al. (2019), Jura et al. (2007) (IR excess)	He	0.6	13594	8.02	Y
GD424	Izquierdo et al. (2020)	He	0.77	16560	8.25	N
GD56	Gianninas et al. (2011), IR excess from Jura et al. (2007)	H	0.67	15270	8.09	Y
GD61	Farihi et al. (2011)	He	0.71	17280	8.2	Y
HE0106-3253	Xu et al. (2019) (T, logg), Farihi et al. (2010a) (Mass, IR excess)	H	0.62	17350	8.12	Y
HS2253+8023	Klein et al. (2011), IR excess absence from Farihi et al. (2009)	He	0.84	14400	8.4	N
LHS2534	Hollands et al. (2021)	He	0.55	4780	7.97	N
NLTT43806	Kilic et al. (2020), IR excess from Farihi et al. (2009)	H	0.704	5838	8.186	N
PG0843+516	Koester et al. (2014), Xu & Jura (2012) (excess)	H	0.577	22412	7.902	Y
PG1015+161	Kilic et al. (2020), Jura et al. (2007) (IR excess)	H	0.642	19226	8.04	Y
PG1225-079	Klein et al. (2011), IR excess from Farihi et al. (2010b)	He	0.58	10800	8	Y
SDSSJ0512-0505	Harrison et al. (2021), mass from MWDD (Dufour et al. 2017). Unable to find mention of IR excess, so assume absent	He	0.803	5560	8.05	N
SDSSJ0738+1835	Dufour et al. (2012), IR excess from Dufour et al. (2010)	He	0.841	13950	8.4	Y
SDSSJ0823+0546	Harrison et al. (2021). Unable to find mention of IR excess, so assume absent. Unable to find value for Mass, so assuming a typical value	He	0.6	5920	7.945	N
SDSSJ0845+2257	Wilson et al. (2015)	He	0.679	19780	8.18	Y
SDSSJ1043+0855	Tremblay et al. (2011). IR excess from Farihi et al. (2010a)	H	0.65	18320	8.05	Y

SDSSJ1228+1040	Tremblay et al. (2011) (mass), IR excess from Brinkworth et al. (2009), others from Gänsicke et al. (2012)	H	0.73	20900	8.15	Y
SDSSJ1242+5226	Raddi et al. (2015)	He	0.59	13000	8	N
SDSSJ2047-1259	Hoskin et al. (2020)	He	0.617	17970	8.04	N
WD0122-227	Swan et al. (2019)	He	0.61	8380	8.06	N
WD0446-255	Swan et al. (2019)	He	0.58	10120	8	N
WD0449-259	Swan et al. (2019)	He	0.61	9850	8.04	N
WD1145+017	Fortin-Archambault et al. (2020), IR excess from Vanderburg et al. (2015)	He	0.656	14500	8.11	Y
WD1145+288	Xu et al. (2019) (T, logg), Kleinman et al. (2012) (Mass), Barber et al. (2014) (IR excess)	H	0.685	12140	8.14	Y
WD1232+563	Coutu et al. (2019), IR excess from Xu et al. (2019)	He	0.77	11787	8.3	Y
WD1350-162	Swan et al. (2019)	He	0.6	11640	8.02	N
WD1425+540	Bergeron et al. (2011), IR excess absence from Xu et al. (2017)	He	0.56	14490	7.95	N
WD1536+520	Farihi (2016), IR excess - identified as candidate by Debes et al. (2011), confirmed by Barber et al. (2014)	He	0.58	20800	7.96	Y
WD1551+175	Xu et al. (2019), Bergeron et al. (2011) (Mass), Bergfors et al. (2014) (IR excess)	He	0.57	14756	8.02	Y
WD2105-820	Swan et al. (2019)	H	0.86	10890	8.41	N
WD2115-560	Swan et al. (2019)	H	0.58	9600	7.97	Y
WD2157-574	Swan et al. (2019)	H	0.63	7010	8.06	N
WD2207+121	Coutu et al. (2019), IR excess from Xu & Jura (2012)	He	0.57	14752	7.97	Y
WD2216-657	Swan et al. (2019)	He	0.61	9120	8.05	N
WDJ1814-7354	González Egea et al. (2020)	H	0.59	10090	8	Y

Table A2: Elemental abundances used in our modelling. Hx refers to the dominant component in the white dwarf atmosphere, either H or He as appropriate. Superscripted indices in the System column indicate the source and any additional notes; see table notes for details.

System	log(Al/Hx)	log(Ti/Hx)	log(Ca/Hx)	log(Ni/Hx)	log(Fe/Hx)	log(Cr/Hx)	log(Mg/Hx)	log(Si/Hx)	log(Na/Hx)	log(O/Hx)	log(C/Hx)	log(N/Hx)
G166-58[a]	-	-	-9.33 ± 0.08	-9.5 ± 0.2	-8.22 ± 0.13	-	-8.06 ± 0.05	<-8.2	-	-	-	-
G241-6[b,1]	<-7.7	-8.97 ± 0.1	-7.3 ± 0.2	-8.15 ± 0.4	-6.82 ± 0.14	-8.46 ± 0.1	-6.26 ± 0.1	-6.62 ± 0.2	-	-5.64 ± 0.11	-	-
G29-38[c,2]	<-6.1	-7.9 ± 0.16	-6.58 ± 0.12	<-7.3	-5.9 ± 0.1	-7.51 ± 0.12	-5.77 ± 0.13	-5.6 ± 0.17	<-6.7	-5 ± 0.12	-6.9 ± 0.12	<-5.7

GALEX1931+0117[d,3]	-6.2 ± 0.2	-	-	-6.7 ± 0.3	-4.5 ± 0.3	-6.1 ± 0.3	-	-4.75 ± 0.2	-	-4.1 ± 0.3	-	-
GALEX1931+0117[e]	-	-	-6.11 ± 0.05	-	-4.43 ± 0.09	-	-4.42 ± 0.06	-4.24 ± 0.07	-	-3.62 ± 0.05	-	-
GALEX1931+0117[f,3]	<-5.85	<-7	-5.83 ± 0.1	<-5.6	-4.1 ± 0.1	-5.92 ± 0.14	-4.1 ± 0.1	-4.35 ± 0.11	-	-3.68 ± 0.1	-	-
GALEXJ2339[g,4]	<-7.7	-9.58 ± 0.4	-8.03 ± 0.75	<-8	-6.99 ± 0.3	-8.73 ± 0.26	-6.58 ± 0.14	-6.59 ± 0.08	<-8	-5.52 ± 0.05	-	-
GD362[h,5]	-6.4 ± 0.2	-7.95 ± 0.1	-6.24 ± 0.1	-7.07 ± 0.15	-5.65 ± 0.1	-7.41 ± 0.1	-5.98 ± 0.25	-5.84 ± 0.3	-7.79 ± 0.2	<-5.14	-	<-4.14
GD378[g,6]	<-7.7	-10.13 ± 0.46	-8.7 ± 0.76	<-8.3	-7.51 ± 0.36	-9.72 ± 0.68	-7.44 ± 0.2	-7.49 ± 0.12	<-7.2	-6.04 ± 0.31	-	-
GD40[b,7]	-7.35 ± 0.12	-8.61 ± 0.2	-6.9 ± 0.2	-7.84 ± 0.26	-6.47 ± 0.12	-8.31 ± 0.16	-6.2 ± 0.16	-6.44 ± 0.3	-	-5.62 ± 0.1	-	-
GD424[i,8]	-6.3 ± 0.1	-7.78 ± 0.09	-6.15 ± 0.05	-6.93 ± 0.1	-5.53 ± 0.12	-7.19 ± 0.07	-5.15 ± 0.04	-5.29 ± 0.04	<-6.5	-4.59 ± 0.12	-	-
GD56[a]	-	-	-6.86 ± 0.2	-	-5.44 ± 0.2	-	-5.55 ± 0.2	-5.69 ± 0.2	-	-	-	-
GD61[j,9]	<-7.8	<-8.6	-7.9 ± 0.0634	<-8.8	-7.6 ± 0.0667	<-8.0	-6.69 ± 0.0467	-6.82 ± 0.0367	<-6.8	-5.95 ± 0.0434	-	-
HE0106-3253[a]	-	-	-5.93 ± 0.11	-	-4.7 ± 0.06	-	-5.57 ± 0.2	-5.48 ± 0.05	-	-	-	-
HS2253+8023[k,10]	<-6.7	-8.74 ± 0.04	-7 ± 0.1	-7.32 ± 0.2	-6.17 ± 0.05	-8 ± 0.06	-6.12 ± 0.08	-6.28 ± 0.06	<-6.8	-5.38 ± 0.12	-	-
LHS2534[l,11]	-	-	-10.08 ± 0.11	-	-9.06 ± 0.08	-10.28 ± 0.06	-8.62 ± 0.06	-	-9.53 ± 0.06	-	-	-
NLTT43806[m]	-7.6 ± 0.17	-9.55 ± 0.14	-7.9 ± 0.19	-9.1 ± 0.17	-7.8 ± 0.17	-9.55 ± 0.22	-7.1 ± 0.13	-7.2 ± 0.14	-8.1 ± 0.14	-	-	-
PG0843+516[d,12]	-6.5 ± 0.2	-	-	-6.3 ± 0.3	-4.6 ± 0.2	-5.8 ± 0.3	-5 ± 0.2	-5.2 ± 0.2	-	-5 ± 0.3	-	-
PG0843+516[a]	-	-	-6.26 ± 0.2	-	-3.84 ± 0.18	-	-4.82 ± 0.2	-4.59 ± 0.12	-	-	-	-
PG1015+161[d,13]	-	-	-6.45 ± 0.2	-	-5.5 ± 0.3	<-5.8	-5.3 ± 0.2	-6.4 ± 0.2	-	-5.5 ± 0.2	-	-
PG1015+161[a]	-	-	-6.4 ± 0.2	-	-4.92 ± 0.2	-	-5.6 ± 0.2	-5.42 ± 0.21	-	-	-	-
PG1225-079[n,14]	<-7.84	-9.45 ± 0.02	-8.06 ± 0.03	-8.76 ± 0.14	-7.42 ± 0.07	-9.27 ± 0.06	-7.5 ± 0.2	-7.45 ± 0.1	<-8.26	<-5.54	-7.8 ± 0.1	-
SDSSJ0512-0505[o,15]	-	-	-8.9 ± 0.1	-	-7.75 ± 0.1	-10 ± 0.2	-7.65 ± 0.1	-	-9.65 ± 0.1	-	-	-
SDSSJ0738+1835[p,16]	-6.39 ± 0.11	-7.95 ± 0.11	-6.23 ± 0.15	-6.31 ± 0.1	-4.98 ± 0.09	-6.76 ± 0.12	-4.68 ± 0.07	-4.9 ± 0.16	-6.36 ± 0.16	-3.81 ± 0.19	-	-
SDSSJ0823+0546[o,17]	-	<-10	-9.8 ± 0.1	-8.6 ± 0.1	-7.35 ± 0.1	-	-7.85 ± 0.1	-	-	-	-	-
SDSSJ0845+2257[q,18]	-5.7 ± 0.15	<-7.15	-5.95 ± 0.1	-5.65 ± 0.3	-4.6 ± 0.2	-6.4 ± 0.3	-4.7 ± 0.15	-4.8 ± 0.3	-	-4.25 ± 0.2	-	-
SDSSJ1043+0855[r,19]	-7.06 ± 0.3	<-7.00	-5.96 ± 0.2	-7.38 ± 0.3	-6.15 ± 0.3	<-6.5	-5.11 ± 0.2	-5.33 ± 0.5	-	-4.9 ± 0.2	-	-
SDSSJ1228+1040[d,20]	-5.75 ± 0.2	-	-5.94 ± 0.2	<-6.5	-5.2 ± 0.3	<-6.00	-5.2 ± 0.2	-4.7 ± 0.2	-	-4.55 ± 0.2	-	-
SDSSJ1228+1040[d,21]	-5.75 ± 0.2	-	-5.94 ± 0.2	<-6.5	-5.2 ± 0.3	<-6.00	-5.2 ± 0.2	-5.2 ± 0.2	-	-4.55 ± 0.2	-	-
SDSSJ1242+5226[s,22]	<-6.5	-8.2 ± 0.2	-6.53 ± 0.1	<-7.3	-5.9 ± 0.15	-7.5 ± 0.2	-5.26 ± 0.15	-5.3 ± 0.06	-7.2 ± 0.2	-4.3 ± 0.1	-	<-5.00
SDSSJ2047-1259[t,23]	<-6.5	-	-6.9 ± 0.1	-7.4 ± 0.1	-6.4 ± 0.2	-	-5.6 ± 0.1	-5.6 ± 0.1	-	-4.8 ± 0.1	-	-
WD0122-227[u]	-	-	-10.1 ± 0.1	-	-8.5 ± 0.2	-	-8.5 ± 0.4	<-7.6	-	<-5.2	-	-
WD0446-255[u,24]	-7.3 ± 0.3	-8.8 ± 0.1	-7.4 ± 0.1	-8.2 ± 0.1	-6.9 ± 0.1	-8.5 ± 0.1	-6.6 ± 0.1	-6.5 ± 0.1	-7.9 ± 0.1	-5.8 ± 0.1	-	-
WD0449-259[u,25]	-	-10.7 ± 0.2	-9.1 ± 0.1	-8.4 ± 0.2	-7.9 ± 0.2	-	-8.3 ± 0.4	<-7.3	-	<-6.6	-	-
WD1145+017[v,3]	-6.89 ± 0.2	-8.57 ± 0.2	-7 ± 0.2	-7.02 ± 0.3	-5.61 ± 0.2	-7.92 ± 0.4	-5.91 ± 0.2	-5.89 ± 0.2	-	-5.12 ± 0.35	-	<-7.00
WD1145+288[a]	-	-	-6.88 ± 0.08	-	-5.43 ± 0.2	-	-6 ± 0.2	<-4.7	-	-	-	-

WD1232+563[a,26]	<-7.50	-8.96 ± 0.11	-7.69 ± 0.05	<-7.3	-6.45 ± 0.11	-8.16 ± 0.07	-6.09 ± 0.05	-6.36 ± 0.13	-	-5.14 ± 0.15	-	-
WD1350-162[u,25]	-	-10 ± 0.1	-8.7 ± 0.1	-	-7.1 ± 0.1	-9 ± 0.2	-6.8 ± 0.1	-7.3 ± 0.2	-	-6.2 ± 0.1	-	-
WD1425+540[w,27]	-	-	-9.26 ± 0.1	-9.67 ± 0.2	-8.15 ± 0.14	-	-8.16 ± 0.2	-8.03 ± 0.31	-	-6.62 ± 0.23	-7.29 ± 0.17	-
WD1536+520[x,28]	-5.38 ± 0.15	-6.84 ± 0.15	-5.28 ± 0.15	-	-4.5 ± 0.15	-5.93 ± 0.15	-4.06 ± 0.15	-4.32 ± 0.15	-	-3.4 ± 0.15	<-4.2	-
WD1551+175[a,26]	-6.99 ± 0.15	-8.68 ± 0.11	-6.93 ± 0.07	<-7.5	-6.6 ± 0.1	-8.25 ± 0.07	-6.29 ± 0.05	-6.33 ± 0.1	-	-5.48 ± 0.15	-	-
WD2105-820[u]	-	-	-8.2 ± 0.1	-	-6 ± 0.2	-	-6 ± 0.2	<-5.5	-	-	-	-
WD2115-560[u]	-7.6 ± 0.1	-	-7.4 ± 0.1	-	-6.4 ± 0.1	-	-6.4 ± 0.1	-6.2 ± 0.1	-	<-5.0	<-4.3	<-4.0
WD2157-574[u]	-8.1 ± 0.1	-	-8.1 ± 0.1	-8.8 ± 0.1	-7.3 ± 0.1	-	-7 ± 0.1	-7 ± 0.1	-	<-3.8	<-3.6	<-3.0
WD2207+121[a,26]	-7.08 ± 0.15	-8.84 ± 0.14	-7.4 ± 0.08	-7.55 ± 0.2	-6.46 ± 0.13	-8.16 ± 0.19	-6.15 ± 0.1	-6.17 ± 0.11	-	-5.32 ± 0.15	-	-
WD2216-657[u]	-	-10.6 ± 0.1	-9 ± 0.1	-	-8 ± 0.2	-	-7.1 ± 0.1	<-7	<-8.5	<-6.5	-	-
WDJ1814-7354[y,29]	<-7.3	<-8	-7.22 ± 0.15	<-6.3	-6.06 ± 0.19	-	-6.14 ± 0.08	<-6	<-7.4	-	-	-

- Sources for the abundances quoted here are as follows: (a) Xu et al. (2019), (b) Jura et al. (2012), (c) Xu et al. (2014), (d) Gänsicke et al. (2012), (e) Vennes et al. (2011), as given in Gänsicke et al. (2012), (f) Melis et al. (2011), (g) Klein et al. (2021), (h) Zuckerman et al. (2007), (i) Izquierdo et al. (2020), (j) Farihi et al. (2013), (k) Klein et al. (2011), (l) Hollands et al. (2021), (m) Zuckerman et al. (2011), (n) Klein et al. (2011) and Xu et al. (2013), (o) Harrison et al. (2021), (p) Dufour et al. (2012), (q) Wilson et al. (2015), (r) Melis & Dufour (2016), (s) Raddi et al. (2015), (t) Hoskin et al. (2020), (u) Swan et al. (2019), (v) Fortin-Archambault et al. (2020), (w) Xu et al. (2017), (x) Farihi (2016), (y) González Egea et al. (2020)
- Notes on specific systems: (1) Excluding C (subsolar), N (subsolar), P, S, Cl, Mn, Cu, Ga, Ge; (2) Excluding S, Mn; (3) Excluding C (subsolar); (4) Using larger error in case of asymmetry. Excluding Be, Mn, Li, V; (5) Excluding C (subsolar), Sc, V, Mn, Co, Cu, Sr; (6) Using larger error in case of asymmetry. Excluding Be, P, S, Mn, Li, V, C (subsolar), N (subsolar); (7) Using larger error in case of asymmetry. Excluding C (subsolar), N (subsolar), P, S, Cl, Mn, Cu, Ga, Ge; (8) Using larger error in case of asymmetry, using Keck data where available (and WHT for O); (9) Excluding S, P, Sc, C (subsolar), N (subsolar), using lower Al upper bound, 1 sigma errors calculated to 3sf from 3 sigma errors given and rounded up where necessary; (10) Excluding Mn, Sc, V, Sr; (11) Excluding Li, K; (12) Using favoured stratified abundances for Ca and Mg, excluding P and S. Excluding C (subsolar); (13) Excluding P, S, C (subsolar); (14) Excluding Mn, Sc, V, Sr, S, Zn; (15) Abundances were refitted by Harrison et al. (2021), Si not previously included; (16) Excluding Sc, V, Mn, Co; (17) Abundances were refitted by Harrison et al. (2021), Ti not previously included; (18) Excluding C (subsolar), N (subsolar), S, Sc, Mn; (19) Excluding P, S, Sc, V, Mn, C (subsolar); (20) Excluding P, S, C (subsolar), using favoured strat values, using optical Si abundance; (21) Excluding P, S, C (subsolar), using favoured strat values, using UV Si abundance; (22) Excluding P, S, Sc, V, Mn, C (subsolar); (23) Excluding P, S, C (subsolar), N (subsolar); (24) Excluding Sc, V, Mn, Sr; (25) Excluding very high Na point; (26) Excluding Mn; (27) Excluding N (subsolar). Using model I; (28) Excluding P, S. Errors reported to be typically 0.1 - 0.2 dex; (29) Excluding P, S

Table A3: Results from Bayesian model. Errors given are 1 sigma. N/A indicates that a parameter was not invoked. A description of the parameters is given in Section 2 in the main text. Superscripted indices have the same meaning as in Table A2

System	$[Fe/H]_{index}$	t/Myrs	$\log(d_{formation}/AU)$	$z_{formation}$/AU	f_c	$\log(f_{pol})$	$\log(t_{event}/Yrs)$	P/GPa	f_{O_2} (ΔIW)
G166-58[a]	274^{+462}_{-69}	$0.69^{+8.48}_{-0.68}$	N/A	N/A	N/A	$-7.92^{+0.04}_{-0.04}$	$6.20^{+1.08}_{-2.02}$	N/A	N/A
G241-6[b,1]	320^{+164}_{-72}	$6.45^{+9.19}_{-4.41}$	$0.24^{+0.16}_{-0.22}$	N/A	N/A	$-5.52^{+0.06}_{-0.07}$	$7.24^{+0.41}_{-0.56}$	N/A	N/A
G29-38[c,2]	338^{+126}_{-124}	$0.02^{+2.29}_{-0.02}$	$-1.27^{+0.31}_{-0.39}$	$0.14^{+0.01}_{-0.01}$	N/A	$-4.94^{+0.02}_{-0.02}$	$4.59^{+2.20}_{-2.56}$	N/A	N/A
GALEX1931+0117[d,3]	137^{+462}_{-98}	$0.00^{+1.15}_{-0.00}$	$0.55^{+0.03}_{-0.03}$	N/A	$0.16^{+0.04}_{-0.03}$	$-3.46^{+0.03}_{-0.03}$	$3.94^{+2.54}_{-2.49}$	$45.0^{+9.8}_{-13.3}$	$-2.6^{+0.3}_{-0.2}$

GALEX1931+0117[e]	459^{+250}_{-167}	$0.00^{+1.77}_{-0.00}$	N/A	N/A	N/A	$-3.74^{+0.10}_{-0.10}$	$3.86^{+2.82}_{-2.56}$	N/A	N/A
GALEX1931+0117[f],3	561^{+0}_{-0}	$0.00^{+0.02}_{-0.00}$	$0.43^{+0.04}_{-0.06}$	$0.07^{+0.05}_{-0.04}$	$0.31^{+0.03}_{-0.03}$	$-3.58^{+0.03}_{-0.04}$	$3.07^{+1.52}_{-1.36}$	$51.6^{+5.0}_{-7.2}$	$-2.7^{+0.2}_{-0.1}$
GALEXJ2339[g],4	413^{+178}_{-159}	$1.94^{+2.84}_{-1.02}$	N/A	$0.07^{+0.05}_{-0.05}$	N/A	$-5.42^{+0.03}_{-0.03}$	$5.12^{+2.19}_{-3.44}$	N/A	N/A
GD362[h],5	568^{+180}_{-177}	$0.23^{+0.27}_{-0.15}$	$-0.81^{+0.13}_{-0.23}$	$0.12^{+0.02}_{-0.03}$	N/A	$-5.18^{+0.02}_{-0.03}$	$4.49^{+2.24}_{-2.93}$	N/A	N/A
GD378[g],6	481^{+311}_{-311}	$2.29^{+14.25}_{-1.54}$	N/A	N/A	N/A	$-6.08^{+0.12}_{-0.11}$	$6.11^{+1.46}_{-4.07}$	N/A	N/A
GD40[b],7	369^{+262}_{-187}	$1.90^{+13.58}_{-1.08}$	$-0.57^{+0.36}_{-0.07}$	$0.09^{+0.04}_{-0.05}$	N/A	$-5.38^{+0.06}_{-0.06}$	$6.50^{+1.10}_{-4.39}$	N/A	N/A
GD424[i],8	381^{+141}_{-95}	$5.21^{+19.86}_{-4.61}$	$-0.60^{+0.02}_{-0.01}$	N/A	N/A	$-4.34^{+0.02}_{-0.02}$	$7.13^{+0.57}_{-0.96}$	N/A	N/A
GD56[a]	563^{+263}_{-305}	$0.01^{+3.17}_{-0.01}$	N/A	N/A	N/A	$-5.06^{+0.09}_{-0.09}$	$4.39^{+2.51}_{-2.84}$	N/A	N/A
GD61[j],9	450^{+260}_{-197}	$3.09^{+10.41}_{-2.76}$	$0.30^{+0.12}_{-0.20}$	N/A	$0.03^{+0.01}_{-0.01}$	$-5.83^{+0.02}_{-0.03}$	$6.91^{+0.63}_{-3.55}$	$40.5^{+11.7}_{-18.5}$	$-2.5^{+0.4}_{-0.3}$
HE0106-3253[a]	515^{+282}_{-302}	$0.00^{+1.41}_{-0.00}$	$-1.47^{+0.41}_{-0.34}$	$0.09^{+0.01}_{-0.01}$	$0.60^{+0.06}_{-0.06}$	$-4.56^{+0.04}_{-0.04}$	$4.09^{+2.45}_{-2.54}$	$25.6^{+18.7}_{-15.5}$	$-1.9^{+0.6}_{-0.6}$
HS2253+8023[k],10	597^{+216}_{-287}	$0.26^{+9.81}_{-0.20}$	$-0.44^{+0.64}_{-0.16}$	N/A	N/A	$-5.19^{+0.07}_{-0.06}$	$6.04^{+1.35}_{-3.83}$	N/A	N/A
LHS2534[l],11	926^{+22}_{-15}	$4.71^{+8.56}_{-0.85}$	$0.55^{+0.02}_{-0.02}$	N/A	$0.52^{+0.14}_{-0.12}$	$-8.38^{+0.03}_{-0.03}$	$3.62^{+3.66}_{-2.30}$	$35.7^{+14.8}_{-16.5}$	$-1.3^{+0.2}_{-0.2}$
NLTT43806[m]	817^{+110}_{-272}	$0.78^{+10.53}_{-0.75}$	$-0.16^{+0.35}_{-0.30}$	$0.10^{+0.04}_{-0.06}$	$0.03^{+0.01}_{-0.01}$	$-6.56^{+0.05}_{-0.05}$	$6.34^{+1.07}_{-2.52}$	$45.6^{+9.7}_{-15.0}$	$-2.7^{+0.4}_{-0.2}$
PG0843+516[d],12	417^{+280}_{-210}	$0.01^{+1.81}_{-0.01}$	$-0.07^{+0.35}_{-0.29}$	N/A	$0.64^{+0.08}_{-0.09}$	$-4.25^{+0.09}_{-0.08}$	$4.13^{+2.50}_{-2.55}$	$29.3^{+21.1}_{-17.1}$	$-2.5^{+0.6}_{-0.3}$
PG0843+516[a]	463^{+313}_{-295}	$0.00^{+1.50}_{-0.00}$	$-0.01^{+0.36}_{-0.38}$	N/A	$0.75^{+0.08}_{-0.10}$	$-3.77^{+0.12}_{-0.12}$	$3.97^{+2.64}_{-2.40}$	$25.8^{+18.7}_{-15.0}$	$-1.9^{+0.6}_{-0.7}$
PG1015+161[d],13	377^{+350}_{-232}	$0.00^{+1.12}_{-0.00}$	$-1.30^{+0.42}_{-0.44}$	$0.11^{+0.02}_{-0.02}$	$0.34^{+0.13}_{-0.12}$	$-5.00^{+0.10}_{-0.09}$	$3.79^{+2.68}_{-2.31}$	$17.8^{+19.0}_{-11.5}$	$-1.7^{+0.4}_{-0.7}$
PG1015+161[a]	499^{+293}_{-316}	$0.00^{+1.27}_{-0.00}$	$-1.09^{+0.56}_{-0.55}$	$0.11^{+0.02}_{-0.03}$	$0.59^{+0.11}_{-0.13}$	$-4.72^{+0.12}_{-0.12}$	$3.98^{+2.57}_{-2.51}$	$31.9^{+17.4}_{-18.8}$	$-2.0^{+0.6}_{-0.6}$
PG1225-079[n],14	494^{+260}_{-250}	$1.49^{+2.71}_{-1.00}$	$-0.87^{+0.21}_{-0.32}$	$0.12^{+0.02}_{-0.04}$	N/A	$-6.93^{+0.07}_{-0.07}$	$5.74^{+1.56}_{-3.51}$	N/A	N/A
SDSSJ0512-0505[o],15	499^{+305}_{-319}	$3.65^{+1.60}_{-1.35}$	$-1.04^{+0.33}_{-0.55}$	$0.13^{+0.01}_{-0.02}$	$0.54^{+0.17}_{-0.21}$	$-7.38^{+0.06}_{-0.06}$	$3.20^{+2.53}_{-2.04}$	$25.5^{+20.0}_{-16.6}$	$-1.8^{+0.5}_{-0.7}$
SDSSJ0738+1835[p],16	375^{+185}_{-219}	$0.49^{+0.07}_{-0.07}$	$0.10^{+0.27}_{-0.41}$	N/A	$0.44^{+0.07}_{-0.07}$	$-3.79^{+0.07}_{-0.07}$	$2.39^{+1.78}_{-1.51}$	$32.3^{+19.2}_{-19.6}$	$-2.5^{+0.6}_{-0.3}$
SDSSJ0823+0546[o],17	438^{+341}_{-297}	$17.66^{+3.41}_{-3.54}$	$0.03^{+0.34}_{-0.38}$	N/A	$0.96^{+0.02}_{-0.04}$	$-7.23^{+0.06}_{-0.06}$	$3.25^{+2.34}_{-2.05}$	$29.0^{+19.8}_{-18.9}$	$-2.1^{+0.6}_{-0.6}$
SDSSJ0845+2257[q],18	586^{+250}_{-350}	$0.47^{+12.05}_{-0.43}$	$-0.21^{+0.36}_{-0.29}$	N/A	$0.31^{+0.10}_{-0.09}$	$-3.76^{+0.08}_{-0.09}$	$6.23^{+1.17}_{-3.45}$	$28.4^{+19.8}_{-18.2}$	$-2.1^{+0.7}_{-0.6}$

SDSSJ1043+0855[r,19]	342^{+245}_{-178}	$0.00^{+1.92}_{-0.00}$	$-0.22^{+0.51}_{-0.38}$	N/A	N/A	$-4.60^{+0.10}_{-0.09}$	$4.03^{+2.64}_{-2.59}$	N/A	N/A
SDSSJ1228+1040[d,20]	421^{+284}_{-245}	$0.01^{+1.82}_{-0.01}$	$-0.69^{+0.42}_{-0.30}$	$0.12^{+0.02}_{-0.05}$	N/A	$-4.28^{+0.06}_{-0.07}$	$4.11^{+2.55}_{-2.59}$	N/A	N/A
SDSSJ1228+1040[d,21]	486^{+291}_{-270}	$0.00^{+1.77}_{-0.00}$	$-0.90^{+0.25}_{-0.52}$	$0.12^{+0.02}_{-0.04}$	N/A	$-4.38^{+0.08}_{-0.09}$	$3.97^{+2.66}_{-2.68}$	N/A	N/A
SDSSJ1242+5226[s,22]	374^{+111}_{-81}	$4.93^{+0.86}_{-0.39}$	$0.05^{+0.34}_{-0.55}$	N/A	N/A	$-4.32^{+0.05}_{-0.04}$	$4.51^{+1.60}_{-3.09}$	N/A	N/A
SDSSJ2047-1259[t,23]	523^{+297}_{-367}	$0.62^{+0.15}_{-0.12}$	$-0.01^{+0.34}_{-0.41}$	N/A	N/A	$-4.67^{+0.06}_{-0.06}$	$2.83^{+2.18}_{-1.95}$	N/A	N/A
WD0122-227[u]	467^{+311}_{-299}	$7.84^{+6.14}_{-4.78}$	$0.03^{+0.37}_{-0.40}$	N/A	$0.57^{+0.19}_{-0.20}$	$-8.23^{+0.15}_{-0.15}$	$3.96^{+2.92}_{-2.58}$	$29.6^{+19.1}_{-18.7}$	$-2.0^{+0.6}_{-0.6}$
WD0446-255[u,24]	814^{+113}_{-339}	$1.09^{+1.42}_{-0.75}$	$-0.58^{+0.13}_{-0.11}$	$0.13^{+0.01}_{-0.02}$	$0.05^{+0.02}_{-0.02}$	$-5.62^{+0.05}_{-0.04}$	$4.54^{+2.42}_{-3.05}$	$36.9^{+15.5}_{-22.5}$	$-2.2^{+0.6}_{-0.5}$
WD0449-259[u,25]	581^{+267}_{-387}	$7.11^{+5.58}_{-4.28}$	$-1.03^{+0.94}_{-0.61}$	$0.10^{+0.03}_{-0.04}$	$0.65^{+0.18}_{-0.23}$	$-7.47^{+0.14}_{-0.15}$	$3.99^{+2.70}_{-2.53}$	$19.9^{+19.3}_{-13.1}$	$-1.4^{+0.3}_{-0.7}$
WD1145+017[v,3]	640^{+214}_{-327}	$0.54^{+8.70}_{-0.39}$	$0.13^{+1.31}_{-0.44}$	N/A	N/A	$-4.87^{+0.32}_{-0.12}$	$5.90^{+1.50}_{-3.78}$	N/A	N/A
WD1145+288[a]	502^{+285}_{-297}	$0.01^{+1.47}_{-0.01}$	$-0.96^{+1.21}_{-0.58}$	$0.12^{+0.02}_{-0.04}$	$0.48^{+0.14}_{-0.15}$	$-5.30^{+0.14}_{-0.12}$	$4.16^{+2.41}_{-2.57}$	$31.7^{+17.5}_{-19.9}$	$-2.0^{+0.6}_{-0.6}$
WD1232+563[a,26]	559^{+0}_{-0}	$13.26^{+24.86}_{-9.00}$	N/A	N/A	N/A	$-5.10^{+0.02}_{-0.03}$	$7.49^{+0.34}_{-0.44}$	N/A	N/A
WD1350-162[u,25]	161^{+440}_{-114}	$6.84^{+1.25}_{-1.13}$	$0.00^{+0.31}_{-0.33}$	N/A	$0.42^{+0.08}_{-0.08}$	$-6.04^{+0.06}_{-0.06}$	$3.11^{+2.28}_{-2.02}$	$22.7^{+22.7}_{-14.9}$	$-2.1^{+0.7}_{-0.6}$
WD1425+540[w,27]	470^{+295}_{-275}	$1.34^{+4.38}_{-0.82}$	N/A	N/A	N/A	$-6.59^{+0.10}_{-0.08}$	$5.48^{+1.90}_{-3.73}$	N/A	N/A
WD1536+520[x,28]	445^{+294}_{-232}	$0.19^{+8.80}_{-0.14}$	$0.10^{+0.29}_{-0.40}$	N/A	N/A	$-3.26^{+0.08}_{-0.07}$	$5.79^{+1.54}_{-3.78}$	N/A	N/A
WD1551+175[a,26]	589^{+171}_{-221}	$4.19^{+20.66}_{-3.44}$	$-0.66^{+0.01}_{-0.01}$	N/A	N/A	$-5.38^{+0.03}_{-0.04}$	$7.08^{+0.64}_{-4.24}$	N/A	N/A
WD2105-820[u]	210^{+486}_{-159}	$0.00^{+0.08}_{-0.00}$	$0.07^{+0.29}_{-0.35}$	N/A	$0.84^{+0.11}_{-0.26}$	$-5.96^{+0.14}_{-0.13}$	$1.53^{+3.79}_{-0.98}$	$18.8^{+21.4}_{-12.6}$	$-1.7^{+0.4}_{-0.7}$
WD2115-560[u]	472^{+217}_{-181}	$0.00^{+0.30}_{-0.00}$	$0.20^{+1.10}_{-0.47}$	N/A	N/A	$-5.84^{+0.04}_{-0.04}$	$3.20^{+2.73}_{-1.74}$	N/A	N/A
WD2157-574[u]	364^{+275}_{-199}	$0.01^{+2.44}_{-0.00}$	N/A	N/A	N/A	$-6.55^{+0.04}_{-0.04}$	$3.09^{+3.70}_{-2.18}$	N/A	N/A
WD2207+121[a,26]	673^{+214}_{-438}	$5.42^{+22.74}_{-4.17}$	$0.12^{+0.28}_{-0.43}$	N/A	N/A	$-5.22^{+0.06}_{-0.06}$	$7.13^{+0.62}_{-4.58}$	N/A	N/A
WD2216-657[u]	388^{+345}_{-272}	$7.18^{+0.97}_{-0.97}$	$-0.18^{+0.28}_{-0.21}$	$0.07^{+0.06}_{-0.05}$	N/A	$-7.25^{+0.04}_{-0.05}$	$3.18^{+2.34}_{-2.09}$	N/A	N/A
WDJ1814-7354[y,29]	382^{+199}_{-147}	$0.02^{+3.22}_{-0.02}$	N/A	N/A	N/A	$-5.94^{+0.04}_{-0.05}$	$4.76^{+2.15}_{-2.43}$	N/A	N/A

Table A4: Results from Bayesian model. N/A indicates that a parameter was not invoked, or (for the category column) that another data set was used for that system. Category abbreviations are as follows: HPM = High Pressure Mantle-rich, LPC = Low Pressure Core-rich, PD = Pressure degenerate with oxygen fugacity, PU = Pressure unconstrained, NED = No Evidence of Differentiation, U = Unphysical. * Previously explained as crust-rich. † May be subject to a degeneracy which causes high pressure fragments to appear to be low pressure; see section 4.5.3. Superscripted indices have the same meaning as in Table A2

System	Good Fit?	Primitive?	Core Rich?	Mantle Rich?	Volatile Rich?	Volatile Depleted?	Moderate Volatile Depleted?	Temperature	Inferred Parent Core Number Fraction	Differentiation Sigma	Category
G166-58[a]	Y	Y	N	N	Y	N	N	N/A	N/A	N/A	NED
G241-6[b,1]	Y	Y	N	N	Y	N	N	223	N/A	N/A	NED
G29-38[c,2]	Y	Y	N	N	N	N	Y	1952	N/A	N/A	NED
GALEX1931+0117[d,3]	N	N	Y	N	Y	N	N	130	0.01	2.7	N/A
GALEX1931+0117[e]	N	N	Y	N	Y	N	N	150	0.14	4.9	NED
GALEX1931+0117[f,3]	N	Y	N	N	Y	N	N	N/A	N/A	N/A	N/A
GALEXJ2339[g,4]	Y	Y	N	N	Y	N	N	N/A	N/A	N/A	NED
GD362[h,5]	Y	Y	N	N	N	N	Y	1516	N/A	N/A	NED
GD378[g,6]	Y	Y	N	N	Y	N	N	N/A	N/A	N/A	NED
GD40[b,7]	Y	Y	N	N	N	Y	N	1197	N/A	N/A	NED
GD424[i,8]	N	Y	N	N	N	Y	N	1268	N/A	N/A	NED
GD56[a]	Y	Y	N	N	Y	N	N	N/A	N/A	N/A	NED
GD61[j,9]	Y	N	N	Y	Y	N	N	198	0.16	1.3	HPM
HE0106-3253[a]	Y	N	Y	N	N	N	Y	2170	0.04	9.2	PD
HS2253+8023[k,10]	Y	Y	N	N	Y	N	N	912	N/A	N/A	NED
LHS2534[l,11]	Y	N	Y	N	Y	N	N	130	0.0	4.3	U
NLTT43806[m]	Y	N	N	Y	Y	N	N	514	0.17	2.8	HPM*
PG0843+516[d,12]	N	N	Y	N	Y	N	N	429	0.17	4.6	N/A
PG0843+516[a]	Y	N	Y	N	Y	N	N	373	0.13	5.6	PD
PG1015+161[d,13]	N	N	Y	N	N	N	Y	1976	0.07	1.4	N/A
PG1015+161[a]	Y	N	Y	N	N	N	Y	1761	0.1	3.3	PD

PG1225-079[n,14]	Y	Y	N	N	N	N	Y	1570	N/A	N/A	NED
SDSSJ0512-0505[o,15]	Y	N	Y	N	N	N	Y	1714	0.1	2.1	PD
SDSSJ0738+1835[p,16]	Y	N	Y	N	Y	N	N	299	0.15	2.9	PU
SDSSJ0823+0546[o,17]	Y	N	Y	N	Y	N	N	349	0.13	10.1	PU
SDSSJ0845+2257[q,18]	Y	N	Y	N	Y	N	N	565	0.14	1.6	PU
SDSSJ1043+0855[r,19]	N	Y	N	N	Y	N	N	587	N/A	N/A	NED
SDSSJ1228+1040[d,20]	Y	Y	N	N	N	N	Y	1419	N/A	N/A	N/A
SDSSJ1228+1040[d,21]	Y	Y	N	N	N	N	Y	1588	N/A	N/A	NED
SDSSJ1242+5226[s,22]	Y	Y	N	N	Y	N	N	330	N/A	N/A	NED
SDSSJ2047-1259[t,23]	Y	Y	N	N	Y	N	N	376	N/A	N/A	NED
WD0122-227[u]	Y	N	Y	N	Y	N	N	349	0.1	2.2	PU
WD0446-255[u,24]	Y	N	N	Y	N	Y	N	1217	0.15	N/A	HPM
WD0449-259[u,25]	Y	N	Y	N	N	N	Y	1711	0.1	N/A	LPC
WD1145+017[v,3]	Y	Y	N	N	Y	N	N	279	N/A	N/A	NED
WD1145+288[a]	Y	N	Y	N	N	N	Y	1642	0.16	1.5	PU
WD1232+563[a,26]	N	Y	N	N	Y	N	N	N/A	N/A	N/A	NED
WD1350-162[u,25]	Y	N	Y	N	Y	N	N	364	0.09	N/A	LPC[†]
WD1425+540[w,27]	Y	Y	N	N	Y	N	N	N/A	N/A	N/A	NED
WD1536+520[x,28]	Y	Y	N	N	Y	N	N	300	N/A	N/A	NED
WD1551+175[a,26]	Y	Y	N	N	N	Y	N	1395	N/A	N/A	NED
WD2105-820[u]	Y	N	Y	N	Y	N	N	318	0.09	N/A	LPC
WD2115-560[u]	Y	Y	N	N	Y	N	N	242	N/A	N/A	NED
WD2157-574[u]	Y	Y	N	N	Y	N	N	N/A	N/A	N/A	NED
WD2207+121[a,26]	Y	Y	N	N	Y	N	N	287	N/A	N/A	NED
WD2216-657[u]	N	Y	N	N	Y	N	N	540	N/A	N/A	NED
WDJ1814-7354[y,29]	Y	Y	N	N	Y	N	N	N/A	N/A	N/A	NED

Table A5: Summary of coefficients used in parametrisations of partitioning behaviour. For coefficients sourced from Fischer et al. (2015), those marked with † are results quoted from epsilon modelling. *S partitioning was implemented following the procedure described by Boujibar et al. (2014), but was not included when running the model on white dwarf systems.

Element	Valence	a	b /K	c /K GPa^{-1}	d	Source	Equation Used
Fe	2	0	0	0	0	N/A	(4)
Mn	2	-0.02	-5600	38	0.036	Corgne et al. (2008)	(2)
Ni	2	0.46	2700	-61	0	Fischer et al. (2015)	(3)
Cr	2	-0.3	-2200	-5	0	Fischer et al. (2015) †	(3)
Ga	3	3.5	-4800	-126	-0.97	Corgne et al. (2008)	(2)
Si	4	0.549	-12324	0	0	Siebert et al. (2013)	(2)
Nb	5	4.09	-15500	-166	-0.75	Corgne et al. (2008)	(2)
Ta	5	7.74	-20000	-264	-1.69	Corgne et al. (2008)	(2)
Cu	1	0.3	2300	-37	0.14	Corgne et al. (2008)	(2)
Zn	2	-1.11	600	-23	-0.21	Corgne et al. (2008)	(2)
V	3	-1.5	-2300	9	0	Fischer et al. (2015) †	(3)
Co	2	0.36	1500	-33	0	Fischer et al. (2015)	(3)
P	5	0.64	-1593	-74.95	0	Wade & Wood (2005)	(2)
Tl	1	-0.118	-783	0	0	Wood et al. (2008)	(2)
W	4.52	3.2	-1605	-115	-0.85	Cottrell et al. (2009)	(2)
O	-2	0.986	-3275	0	0	Siebert et al. (2013)	(2)
C	4	-1	4842	31	0	Blanchard et al. (2019)	(3)
S	-2	0	405	136	0	Boujibar et al. (2014)	N/A *

Table A6: Tabulated extract of Figure 15, showing predicted elemental abundances in a white dwarf atmosphere as a function of the core fraction of a pollutant fragment and the core–mantle differentiation pressure in its parent. Hx represents the dominant element in the white dwarf atmosphere, either H or He. Mg/Fe and Ca/Fe act as proxies for the fragment core fraction. When this quantity is known, Cr, Ni and/or Si can be used to infer pressure. Note that this table assumes steady-state accretion and heavy pollution (meaning that the total pollution of the elements we model varies between -3 and -4 log units relative to Hx) - see caption of Figure 15 and the main text for further details.

Fragment Core Fraction	Pressure /GPa	log(Mg/Fe)	log(Ca/Fe)	log(Cr/Hx)	log(Ni/Hx)	log(Si/Hx)
0	0	0.99	-0.06	-7.15	-9.19	-5.05
0	10	1.0	-0.05	-7.2	-8.67	-5.06
0	20	1.01	-0.04	-7.23	-8.39	-5.06
0	30	1.03	-0.03	-7.26	-8.16	-5.07
0	40	1.06	0.0	-7.3	-7.99	-5.09
0	50	1.1	0.04	-7.36	-7.85	-5.12
0	60	1.13	0.07	-7.42	-7.73	-5.14
0.2	0	0.06	-0.99	-7.24	-6.74	-5.27
0.2	10	0.07	-0.98	-7.22	-6.74	-5.26
0.2	20	0.08	-0.97	-7.22	-6.75	-5.26
0.2	30	0.1	-0.96	-7.21	-6.77	-5.25
0.2	40	0.13	-0.93	-7.21	-6.79	-5.24
0.2	50	0.17	-0.89	-7.22	-6.81	-5.22
0.2	60	0.2	-0.85	-7.23	-6.84	-5.22
0.4	0	-0.33	-1.39	-7.31	-6.53	-5.49
0.4	10	-0.32	-1.38	-7.24	-6.54	-5.47
0.4	20	-0.31	-1.37	-7.21	-6.54	-5.45
0.4	30	-0.29	-1.35	-7.19	-6.56	-5.41
0.4	40	-0.27	-1.32	-7.16	-6.58	-5.37
0.4	50	-0.23	-1.28	-7.14	-6.6	-5.31
0.4	60	-0.19	-1.25	-7.12	-6.62	-5.28
0.6	0	-0.67	-1.73	-7.37	-6.43	-5.74
0.6	10	-0.66	-1.72	-7.25	-6.44	-5.7

0.6	20	-0.65	-1.71	-7.21	-6.44	-5.66
0.6	30	-0.63	-1.69	-7.17	-6.45	-5.58
0.6	40	-0.61	-1.66	-7.13	-6.47	-5.49
0.6	50	-0.57	-1.62	-7.09	-6.49	-5.4
0.6	60	-0.53	-1.59	-7.06	-6.51	-5.33
0.8	0	-1.09	-2.15	-7.41	-6.37	-6.1
0.8	10	-1.08	-2.14	-7.25	-6.37	-6.02
0.8	20	-1.07	-2.13	-7.2	-6.38	-5.91
0.8	30	-1.05	-2.11	-7.16	-6.39	-5.77
0.8	40	-1.03	-2.08	-7.11	-6.4	-5.62
0.8	50	-0.99	-2.04	-7.05	-6.42	-5.47
0.8	60	-0.95	-2.01	-7.01	-6.44	-5.38
0.99	0	-2.48	-3.54	-7.45	-6.33	-7.37
0.99	10	-2.47	-3.53	-7.26	-6.34	-6.67
0.99	20	-2.46	-3.52	-7.2	-6.34	-6.3
0.99	30	-2.44	-3.5	-7.15	-6.35	-5.99
0.99	40	-2.42	-3.47	-7.09	-6.36	-5.75
0.99	50	-2.38	-3.43	-7.03	-6.38	-5.54
0.99	60	-2.34	-3.4	-6.98	-6.39	-5.42

APPENDIX B: COMMENTS ON INDIVIDUAL SYSTEMS

B1 GD61

The depletion in Ni and Fe illustrated in Figure 9 suggests that the pollution is rich in mantle-like material. The red line shows how the median fit would change if the pressure was fixed to 0 GPa while using the same posterior distribution for the other parameters. While the difference due to pressure is very much a secondary effect, the fit is noticeably improved at higher pressure. This is driven by Si partitioning and the indirect change in mantle Fe content. Our median model hits the artificial D_{Si} cap, which implies that our pressure constraint could be stronger if we allowed Si to partition more strongly into the core.

The median pressure is 40 GPa, which (given the composition inferred by our model) corresponds to a planet of mass 0.6 $M_{\oplus}$. We illustrate the posterior distribution of pressure in Figure 11, which exhibits a peak between 40 and 60 GPa - i.e., roughly Earth-like pressure, and hence Earth-like mass.

Our results are generally in agreement with previous work by Farihi et al. (2013). We find that GD61 is in a steady-state phase of accretion, which is consistent with Farihi et al. (2013) and the presence of an infra-red excess. Farihi et al. (2013) additionally found that the pollution contained excess O, implying the accretion of water. We follow a similar analysis, computing the amount of O in the parent body's mantle which would be left over if all other components were fully oxidised. Assuming that all remaining O is contained in H_2O, and that the parent body's mass is indeed $0.61 M_{\oplus}$ as implied by our model, we find that there is enough excess O (34% of the mantle's O budget, by number) to account for significant amounts of water. The implied total mass of water in the parent body is $5.1^{+2.1}_{-2.9} \times 10^{23}$ kg, where the error comes from propagating our error on pressure. Farihi et al. (2013) found that GD61 has accreted (at most) 5×10^{19} kg of water (based on the trace H content in the atmosphere of GD61). This discrepancy implies that either our inferred parent body differentiation pressure (and hence mass) is an overestimate, or that GD61 has so far accreted only a very small amount of the parent body's water budget (roughly 0.01%).

B2 WD0446-255

High pressure and low oxygen fugacity is favoured. Compared to the median fit (with pressure = 37^{+15}_{-22} GPa), the log-likelihood is decreased by 0.66 when fixing pressure to 0. All elements, apart from Mg, fit better at high pressure. Cr and Fe show the greatest change with pressure, but as with GD61, the Ni abundance is not strongly affected despite the fragment being mantle-rich. We discuss this behaviour in the Appendix.

The depletion in siderophile elements pushes the model to a mantle rich fragment with 5.5% core. Compared to GD61 it has a low Mg/Fe ratio, only slightly above solar, as shown in Figure 6. However, our model finds that the Mg abundance is anomalously low: the model is able to match the abundance of all 9 other elements modelled to within 1 sigma, but predicts an Mg abundance roughly 2 sigma above that observed. This may be down to random chance: the probability that at least one of the 10 data points is observed at least 2 sigma away from its true value is 37%. The sensitivity to pressure is therefore greater than suggested by Figure 6. To best match the low Mg, the model favours a build-up phase solution. This is consistent with the results of Swan et al. (2019). The high refractory element abundances (and slight O depletion) suggest incomplete condensation.

B3 NLTT43806

Our model finds a good fit to the data by invoking the accretion of mantle-rich material. Again, high pressure is preferred. However, the pollutant has previously been explained as being composed (at least partially) of crust-rich material due to the high Al and Ca abundances (Zuckerman et al. 2011). Our model does not reproduce these Al or Ca observations because we don't include crustal material. We infer that our fit could be further improved by including crustal material, as was found by Harrison et al. (2018).

B4 WD0449-259

The model finds 2 degenerate solutions for this system. The first solution is a highly core-rich fragment, with extreme heating, accreting in build up/steady state. This roughly follows the heating effects arrow from the 80% core contour to the data point in the middle panel of Figure 6. The second solution invokes a less core-rich fragment, with decreased heating, accreting in the declining phase. This is similar to the first solution, but starting at a lower core fraction, and following part of both the heating and sinking arrows to the data point.

Importantly, both solutions favour low pressure (and high oxygen fugacity) in order to make Ni as siderophilic as possible. Given that this is a core-rich fragment (as suggested by the super-solar Fe/Mg and Ni/Mg ratios), moving as much Ni into the core as possible helps to match the high observed Ni/Fe.

Swan et al. (2019) reported an anomalously high Na abundance for this system which our model cannot reproduce. The cause is unknown. We therefore leave open the question of how to explain these anomalous lines and consider only the other observed (or constrained) elements.

B5 WD1350-162

The median model is moderately core-rich (41%), with low pressure favoured by the low Si abundance. The high observed Mg value relative to other elements is explained by accretion in the declining phase. This is consistent with the lack of observed infra-red excess. However, the model seems to also admit a (less favoured) high pressure solution (with additional heating and a slightly higher fragment core fraction). We discuss this important degeneracy in section 4.5.3.

As with WD0449-259, an anomalously high Na abundance was reported for this system by Swan et al. (2019) which we exclude from our modelling.

B6 WD2105-820

This system has a strong requirement for differentiation (>4σ) due to its low Ca/Fe ratio, which suggests a core-rich fragment (84%). Our model explains the comparatively high Mg abundances as being caused by accretion in the declining phase. The preference for low pressure is driven by an upper bound on Si: core-like fragments become more Si rich as pressure increases.

B7 PG0843+516

The model is able to fit this data by the accretion of a core rich fragment (73%), driven by the high Fe relative to Ca, Mg and Si. We find a degeneracy between pressure and oxygen fugacity, which is caused by Si. Increasing pressure makes Si more siderophilic, but

increasing oxygen fugacity makes Si less siderophilic. It's possible to increase (or decrease) both in such a way as to keep the final Si abundance within the errors. Including a Cr or Ni data point may help break the degeneracy.

As noted by Xu et al. (2019), there is a known discrepancy between metal abundances based on UV and optical data. We ran our model on two data sets for this system, taken from Gänsicke et al. (2012) and Xu et al. (2019). Gänsicke et al. (2012) used UV data from HST's COS instrument, and we use their abundances reported for Al, Ni, Fe, Cr, Mg, Si and O. The abundances of Xu et al. (2019) are based on optical data from HIRES at Keck, from which we use Ca, Fe, Mg and Si. The Mg abundances are consistent to within the reported errors, but the Fe and Si abundances are both significantly higher in Xu et al. (2019). Our results are based on the version presented in Xu et al. (2019), because we were unable to simultaneously fit the extreme Cr and Ni abundances in Gänsicke et al. (2012).

It is possible that the material in the WD's photosphere may have been completely recycled in between the UV and optical observations. The sinking timescales for this WD are very short - of the observed elements, the longest sinking timescale belongs to Si (25 days). This implies that the material in the WD's photosphere may have been completely recycled in between the UV and optical observations. However, as a DA white dwarf with $T_{\rm eff}$ $\gtrsim$15,000-18,000 K, our interpolated sinking timescales for this white dwarf should be treated with caution (see section 4.4).

B8 HE0106-3253 and PG1015+161

These systems are similar to PG0843+516: the model infers a core-rich fragment with the only pressure-sensitive element being Si. This leads to a pressure/oxygen fugacity degeneracy. Along with PG0843+516, they appear towards the bottom left of the bottom panel in Figure 6, in the region where Si is reasonably sensitive to pressure. This suggests that these objects would potentially yield tight pressure constraints, if another element were present to break the pressure/oxygen fugacity degeneracy.

PG1015+161 has multiple data sets, from Gänsicke et al. (2012) and Xu et al. (2019). As with PG0843+516, we use the set from Xu et al. (2019) since the model is unable to fit the data from Gänsicke et al. (2012) (in particular, the low Si/Mg ratio is difficult to reconcile with the other detected abundances).

B9 SDSSJ0512-0505

This system has roughly solar Fe/Mg and Ca/Mg ratios, but a depletion in Cr, which the model can explain as the accretion of a primarily core-rich fragment. To match the low Cr/Fe ratio, the model reduces the partition coefficient of Cr. It can do this by either lowering pressure or increasing oxygen fugacity, leading to a degeneracy.

B10 SDSSJ0823+0546

Our model finds that SDSSJ0823+0546 has accreted a core-rich (96%) fragment. The only pressure-sensitive element detected is Ni. As discussed in section 2.4, Ni is typically poor for constraining the pressure of core-rich fragments, and we correspondingly find that the model is unable to constrain pressure. A Si detection would strongly constrain pressure: our model predicts that the Si abundance would vary by more than an order of magnitude across the range of pressures we consider.

B11 SDSSJ0738+1835

Cr, Ni and Si are all present, but the model can't constrain pressure because it finds multiple high-likelihood regions of parameter space, leading to a bimodal pressure distribution. All of these solutions invoke accretion of a moderately core-rich fragment (44%) in the declining phase. However, there are 3 possible combinations of pressure, oxygen fugacity and stellar metallicity. Two of these solutions invoke high pressure, while the other invokes low pressure.

B12 SDSSJ0845+2257

Pressure could not be constrained for this system due to a combination of both the large error bars and the inference that the fragment is only slightly core-rich (33%), reducing the effect of changing pressure.

B13 WD0122-227 and WD1145+288

WD0122-227 and WD1145+288 are polluted by core-rich fragments, but in each case the only potential for information about pressure comes from an upper bound on Si. Since these upper bounds are not strong, pressure is unconstrained.

B14 LHS2534

The model was able to fit the data, but the result was deemed unphysical. The median model corresponds to a parent body composed of mostly O (79%), with very low Fe content (6%) - consequently it has an unrealistically small core. This behaviour is a consequence of moving to an unusually high metallicity/high formation distance part of parameter space. Hollands et al. (2021) concluded that this system was polluted by crustal material. We don't consider crustal material in our model, which may explain why we were unable to find a satisfactory fit to the data. We also note that this object is magnetic, which complicates spectral analysis (Hollands et al. 2021).

B15 GALEX1931+0117

We adopted data from Gänsicke et al. (2012) for this system, from which we found no evidence of differentiation. However, data were also available from Vennes et al. (2011) and Melis et al. (2011). The fit to the data from Vennes et al. (2011) was deemed to be unphysical, with a parent body composed of mostly O (89%) and low Fe (3%), similar to LHS2534. This was likely driven by the relative enrichment in Si and O compared to the other data sets. The data set from Melis et al. (2011) has a low Ca/Mg ratio which the model was unable to fit given that the short sinking timescales effectively restrict it to steady state accretion, and that the O abundance constrains the effect of incomplete condensation. Melis et al. (2011) suggested that the abundances may be explained by accretion of a parent body which has been stripped of its crust (and most of its mantle) by the AGB stellar wind. Similarly, Harrison et al. (2018) found that their fit to the data was improved if the parent body had a large crust which was removed by collisions. Our inability to fit this dataset may be because we don't include selective depletion of

crustal material. We also note that our sinking timescales for hot DAs such as this may not be accurate (see 4.4).

APPENDIX C: PREDICTED CORE/MANTLE COMPOSITION

In this section, we show predictions for the core and mantle composition of an Earth-like body which forms under different pressure/oxygen fugacity conditions. Figure C1 illustrates the change in number abundance of various elements in the core and mantle as a function of pressure and oxygen fugacity. In each panel, the vertical thickness of each shaded segment indicates the abundance (by number) of the corresponding element. The top panels show both the core (hatched area) and mantle (unhatched area) compositions. Our model predicts that the core number fraction increases with increasing pressure (as Si and O partition more strongly into the core) and decreases with increasing oxygen fugacity (as metallic Fe is oxidised and incorporated into the mantle).

The behaviour discussed in section 2.4 is visible in Figure C1. In the left-hand middle panel, the dark blue strip shows the mantle abundance of Ni, which increases significantly with increasing pressure (as Ni becomes less siderophilic). In contrast, the core abundance of Ni (shown in the lower left-hand panel) changes very little. The lower left-hand panel also shows a dramatic increase in core Si (red) as pressure increases, while the mantle abundance remains roughly constant. As pressure increases, the increase in core Cr (pink), as well as the noticeable decrease in mantle Cr, are both visible.

APPENDIX D: PRESSURE SENSITIVITY OF DIFFERENT ELEMENTS

Pressure sensitivity varies by element, and also depends on the overall fragment composition. We wish to calculate how the log bulk number abundance of an element, M, in the fragment, X_b, varies with pressure.

We firstly calculate X_b. For an element differentiating with partition coefficient D, the normalised core number abundance in the parent, N_c is

$$N_c = \frac{N_b D}{Dw + (1-w)}, \tag{D1}$$

where N_b is the normalised bulk number abundance of element M in the parent and w is the parent core number fraction. Similarly, the normalised mantle number abundance in the parent, N_m is

$$N_m = \frac{N_b}{Dw + (1-w)} \tag{D2}$$

The fragment's composition is determined by combining the parent core and mantle material in arbitrary proportions. Taking f to be the fraction of core-like material in the fragment, we find that

$$X_b = \frac{fDN_b + (1-f)N_b}{Dw + (1-w)} \tag{D3}$$

As the pressure changes, D and w also change. Differentiating equation D3 with respect to P gives

$$\frac{dX_b}{dP} = \frac{N_b(f-w)\frac{dD}{dP} - N_b(f(D-1)+1)(D-1)\frac{dw}{dP}}{(1+(D-1)w)^2}, \tag{D4}$$

in which we note that P could be replaced by any variable which affects D and/or w. Note that if the parent core fraction does not vary with P, the right hand side vanishes when $f = w$. In other words, we recover the intuitive result that if the fragment samples the parent's core and mantle in the same proportion as the parent itself, the abundance of M is unaffected. In our model, the parent core fraction generally increases with pressure (i.e., $\frac{dw}{dP} > 0$, see Figure C1), which means that even when $f = w$ the abundance of M varies with pressure.

Elemental observations are typically expressed as log number abundances (base 10), so we now find $\frac{d\log X_b}{dP}$. Using the identity

$$\frac{d\log(X_b)}{dP} = \frac{1}{X_b \ln(10)}\frac{dX_b}{dP} \tag{D5}$$

we find

$$\frac{d\log(X_b)}{dP} = \frac{(f-w)\frac{dD}{dP} - (f(D-1)+1)(D-1)\frac{dw}{dP}}{\ln(10)(f(D-1)+1)(w(D-1)+1} \tag{D6}$$

The greater the magnitude of this quantity, the easier it is to resolve the core–mantle differentiation pressure in the parent body. Observational errors are typically on the order of 0.1 log units, so as a rough order of magnitude estimate we require $|\frac{d\log(X_b)}{dP}| > 0.01\text{GPa}^{-1}$ in order to resolve the pressure to within 10 GPa. This threshold could be lower if multiple elements are detected.

Figure D1 shows how pressure sensitivity changes with fragment core fraction for different elements, assuming a bulk Earth parent composition.

Despite Ni having a partition coefficient which spans many orders of magnitude over the pressures we investigate, it only becomes sensitive to pressure at very low fragment core fractions (≈0.01). This is because the value of f at which $\frac{d\log(X_b)}{dP} = 0$ is reduced by virtue of D_{Ni} being large and decreasing with pressure. Because Ni is highly siderophilic, its abundance in the core is not sensitive to pressure and even a small amount of core-like material overwhelms the mantle's Ni contribution. This is why the Ni abundance of certain systems shows little sensitivity to pressure, despite being polluted by apparently mantle-rich material.

In the context of Figure 6, $\frac{d(\log X_b)}{dP}$ is the quantity which sets how spread apart the pressure contours are at a given fragment core fraction. Since we plot ratios of 2 elements, the contours will additionally be spread apart further (along the relevant axis direction) if the elements have sensitivities with opposite signs (and vice versa). Pressure sensitivity is a function of pressure, which means that along a line of constant fragment core fraction, the pressure contours are not necessarily evenly spaced.

REFERENCES

Barber S. D., Kilic M., Brown W. R., Gianninas A., 2014, The Astrophysical Journal, 786, 77

Becklin E. E., Farihi J., Jura M., Song I., Weinberger A. J., Zuckerman B., 2005, The Astrophysical Journal, 632, L119

Bergeron P., et al., 2011, Astrophysical Journal, 737, 28

Bergfors C., Farihi J., Dufour P., Rocchetto M., 2014, Monthly Notices of the Royal Astronomical Society, 444, 2147

Blanchard I., Jennings E. S., Franchi I. A., Zhao X., Petitgirard S., Miyajima N., submitted 2019, EarthArXiv, pp 1–33

Boujibar A., Andrault D., Bouhifd M. A., Bolfan-Casanova N., Devidal J.-L., Trcera N., 2014, Earth and Planetary Science Letters, 391, 42

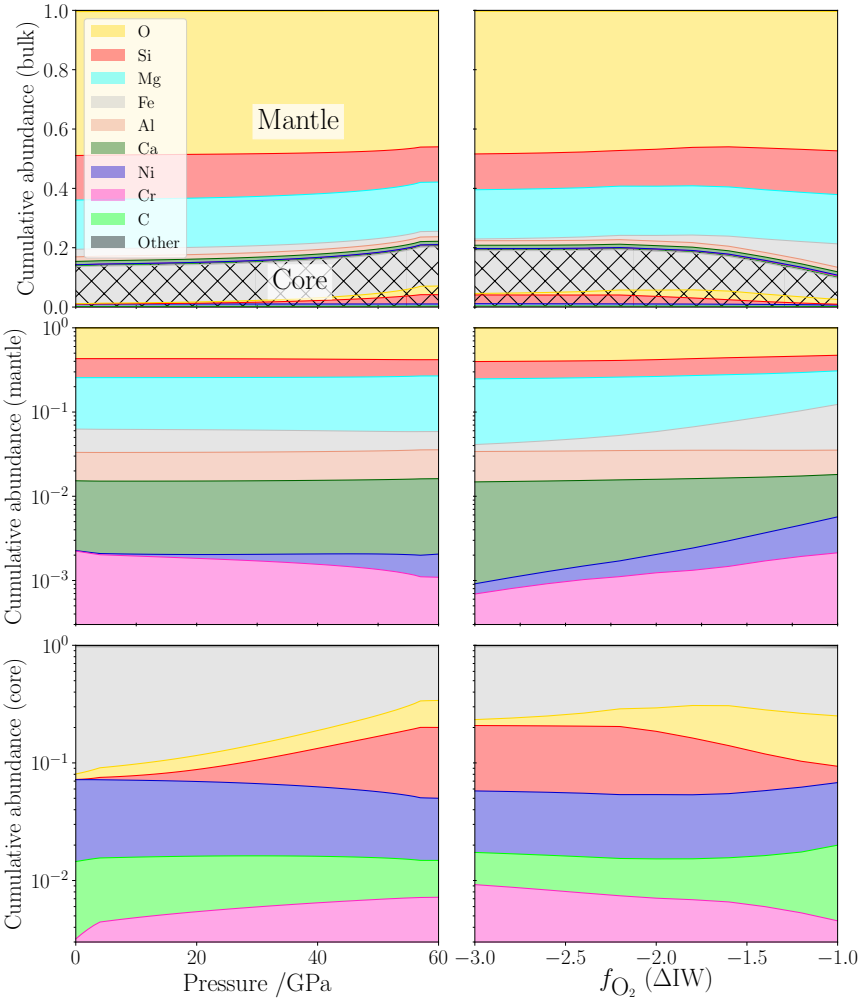

Figure C1. Illustration of the effect of model's predicted elemental partitioning behaviours on the resulting core and mantle composition in the parent body of a White Dwarf pollutant. In each panel, the vertical thickness of each shaded segment indicates the abundance (by number) of the corresponding element. The left hand column of panels shows how the elemental abundances vary with pressure, while the right hand panels show variation with oxygen fugacity (measured relative to the Iron Wüstite buffer). The top panels show both the core (hatched area) and mantle (unhatched area) compositions of a body with bulk Earth composition. The cumulative abundance of elements in the core is equal to the predicted core number fraction, which for reference is approximately 0.17 for Earth. The middle and lower plots show just the mantle and core compositions respectively, with abundances plotted on a log scale (base 10) to better the behaviour of specific elements of interest. See the main text for a discussion of the salient features. When varying pressure, oxygen fugacity was held at IW - 2, and when varying oxygen fugacity the pressure was held at 54 GPa. These figures were chosen to roughly correspond to Earth-like values (Fischer et al. 2015).

Brinkworth C. S., Gänsicke B. T., Marsh T. R., Hoard D. W., Tappert C., 2009, The Astrophysical Journal, 696, 1402

Corgne A., Keshav S., Wood B. J., McDonough W. F., Fei Y., 2008, Geochimica et Cosmochimica Acta, 72, 574

Cottrell E., Walter M. J., Walker D., 2009, Earth and Planetary Science Letters, 281, 275

Coutu S., Dufour P., Bergeron P., Blouin S., Loranger E., Allard N. F., Dunlap B. H., 2019, The Astrophysical Journal, 885, 74

Debes J. H., Hoard D. W., Wachter S., Leisawitz D. T., Cohen M., 2011, The Astrophysical Journal Supplement Series, 197, 38

Dufour P., Kilic M., Fontaine G., Bergeron P., Lachapelle F.-R., Kleinman S. J., Leggett S. K., 2010, The Astrophysical Journal, 719, 803

Dufour P., Kilic M., Fontaine G., Bergeron P., Melis C., Bochanski J., 2012, The Astrophysical Journal, 749, 6

Dufour P., Blouin S., Coutu S., Fortin-Archambault M., Thibeault C., Bergeron P., Fontaine G., 2017, in Tremblay P. E., Gaensicke B., Marsh T., eds, Astronomical Society of the Pacific Conference Series Vol. 509, 20th European White Dwarf Workshop. p. 3 (arXiv:1610.00986)

Farihi J., 2016, New Astronomy Reviews, 71, 9

Farihi J., Zuckerman B., Becklin E. E., 2008, The Astrophysical Journal, 674, 431

Farihi J., Jura M., Zuckerman B., 2009, The Astrophysical Journal, 694, 805

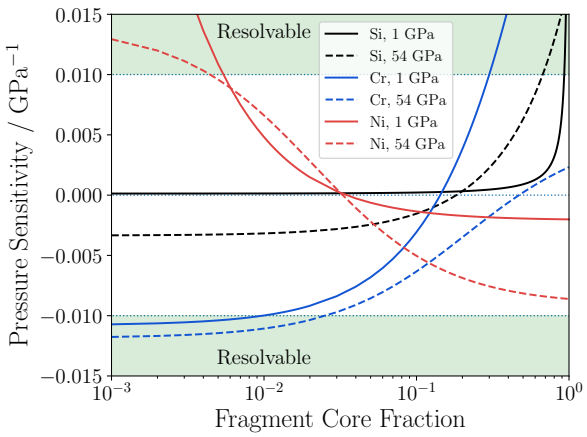

Figure D1. Sensitivity of selected elements to pressure with varying fragment core fraction, calculated using Equation D6. The shaded green regions give an approximate indication of the magnitude of pressure sensitivity which our model can resolve (this threshold could be more generous if multiple elements are present or errors are small). Pure (or nearly pure) core- or mantle-like material is needed in order for pressure induced abundance changes to be resolvable.

Farihi J., Barstow M. A., Redfield S., Dufour P., Hambly N. C., 2010a, Monthly Notices of the Royal Astronomical Society, 404, 2123

Farihi J., Jura M., Lee J.-E., Zuckerman B., 2010b, The Astrophysical Journal, 714, 1386

Farihi J., Brinkworth C. S., Gänsicke B. T., Marsh T. R., Girven J., Hoard D. W., Klein B., Koester D., 2011, The Astrophysical Journal, 728, L8

Farihi J., Gänsicke B. T., Koester D., 2013, Science, 342, 218

Fischer R. A., et al., 2015, Geochimica et Cosmochimica Acta

Fortin-Archambault M., Dufour P., Xu S., 2020, The Astrophysical Journal, 888, 47

Gianninas A., Bergeron P., Ruiz M. T., 2011, Astrophysical Journal, 743, 138

González Egea E., et al., 2020, Monthly Notices of the Royal Astronomical Society, 501, 3916

Gänsicke B. T., Koester D., Farihi J., Girven J., Parsons S. G., Breedt E., 2012, Monthly Notices of the Royal Astronomical Society, 424, 333

Harrison J. H., Bonsor A., Madhusudhan N., 2018, Monthly Notices of the Royal Astronomical Society, 479, 3814

Harrison J. H. D., Bonsor A., Kama M., Buchan A. M., Blouin S., Koester D., 2021, Monthly Notices of the Royal Astronomical Society, 504, 2853–2867

Hollands M. A., Tremblay P.-E., Gänsicke B. T., Koester D., Gentile-Fusillo N. P., 2021, Nature Astronomy, 5, 451–459

Hoskin M. J., et al., 2020, Monthly Notices of the Royal Astronomical Society, 499, 171

Izquierdo P., Toloza O., Gänsicke B. T., Rodríguez-Gil P., Farihi J., Koester D., Guo J., Redfield S., 2020, Monthly Notices of the Royal Astronomical Society, 501, 4276

Jura M., Farihi J., Zuckerman B., 2007, The Astrophysical Journal, 663, 1285

Jura M., Xu S., Klein B., Koester D., Zuckerman B., 2012, Astrophysical Journal, 750, 69

Kilic M., von Hippel T., Leggett S. K., Winget D. E., 2005, The Astrophysical Journal, 632, L115

Kilic M., Bergeron P., Kosakowski A., Brown W. R., Agüeros M. A., Blouin S., 2020, The Astrophysical Journal, 898, 84

Klein B., Jura M., Koester D., Zuckerman B., 2011, The Astrophysical Journal, 741, 64

Klein B. L., Doyle A. E., Zuckerman B., Dufour P., Blouin S., Melis C., Weinberger A. J., Young E. D., 2021, The Astrophysical Journal, 914, 61

Kleinman S. J., et al., 2012, The Astrophysical Journal Supplement Series, 204, 5

Koester D., Gänsicke B. T., Farihi J., 2014, A&A, 566, A34

Leggett S. K., et al., 2018, The Astrophysical Journal Supplement Series, 239, 26

Melis C., Dufour P., 2016, The Astrophysical Journal, 834, 1

Melis C., Farihi J., Dufour P., Zuckerman B., Burgasser A. J., Bergeron P., Bochanski J., Simcoe R., 2011, The Astrophysical Journal, 732, 90

Raddi R., Gänsicke B. T., Koester D., Farihi J., Hermes J. J., Scaringi S., Breedt E., Girven J., 2015, Monthly Notices of the Royal Astronomical Society, 450, 2083

Siebert J., Badro J., Antonangeli D., Ryerson F. J., 2013, Science, 339, 1194

Swan A., Farihi J., Koester D., Hollands M., Parsons S., Cauley P. W., Redfield S., Gänsicke B. T., 2019, Monthly Notices of the Royal Astronomical Society, 490, 202

Tremblay P.-E., Bergeron P., Gianninas A., 2011, The Astrophysical Journal, 730, 128

Vanderburg A., et al., 2015, Nature, 526, 546–549

Vennes S., Kawka A., Németh P., 2010, Monthly Notices of the Royal Astronomical Society: Letters, 404, L40

Vennes S., Kawka A., Németh P., 2011, Monthly Notices of the Royal Astronomical Society, 413, 2545

Wade J., Wood B. J., 2005, Earth and Planetary Science Letters, 236, 78

Wilson D. J., Gaensicke B. T., Koester D., Toloza O., Pala A. F., Breedt E., Parsons S. G., 2015, Monthly Notices of the Royal Astronomical Society, 451, 3237–3248

Wood B. J., Nielsen S. G., Rehkämper M., Halliday A. N., 2008, Earth and Planetary Science Letters, 269, 326

Xu S., Jura M., 2012, The Astrophysical Journal, 745, 88

Xu S., Jura M., Klein B., Koester D., Zuckerman B., 2013, The Astrophysical Journal, 766, 132

Xu S., Jura M., Koester D., Klein B., Zuckerman B., 2014, The Astrophysical Journal, 783, 79

Xu S., Zuckerman B., Dufour P., Young E. D., Klein B., Jura M., 2017, The Astrophysical Journal, 836, L7

Xu S., Dufour P., Klein B., Melis C., Monson N. N., Zuckerman B., Young E. D., Jura M. A., 2019, The Astronomical Journal, 158, 242

Zuckerman B., Becklin E. E., 1987, Nature, 330, 138

Zuckerman B., Koester D., Melis C., Hansen B. M., Jura M., 2007, The Astrophysical Journal, 671, 872

Zuckerman B., Melis C., Klein B., Koester D., Jura M., 2010, Astrophysical Journal, 722, 725

Zuckerman B., Koester D., Dufour P., Melis C., Klein B., Jura M., 2011, The Astrophysical Journal, 739, 101

This paper has been typeset from a TEX/LATEX file prepared by the author.